Influence of substrate surface morphology on powder spreading in laser powder bed fusion process

Wu, Yaping; Chu, Fuzhong; Zhang, Chaocai; Yan, Hongyu; Wang, Lin; Zhou, Zongyan

DOI
10.1016/j.powtec.2025.121296

Publication date
2025

Document Version
Final published version

Published in
Powder Technology

Powder Technology 464 (2025) 121296

Contents lists available at ScienceDirect

Powder Technology

journal homepage: www.journals.elsevier.com/powder-technology

Influence of substrate surface morphology on powder spreading in laser powder bed fusion process☆

Yaping Wu [a], Fuzhong Chu [b], Chaocai Zhang [a], Hongyu Yan [a], Lin Wang [c], Zongyan Zhou [a,b,*]

[a] Jiangxi Provincial Key Laboratory of Particle Technology, Jiangxi University of Science and Technology, Nanchang 330013, China
[b] ARC Research Hub for Smart Process Design and Control, Department of Chemical and Biological Engineering, Monash University, Melbourne, VIC 3800, Australia
[c] Resource & Recycling, Department of Engineering Structures, Faculty of Civil Engineering and Geosciences, Delft University of Technology, 2628, CN, Delft, the Netherlands

HIGHLIGHTS

- Effect of substrate roughness and texture angle on powder bed is investigated.
- Powder bed quality is more influenced by surface roughness than texture angle.
- Aligning powder spreading direction at 90° to texture can improve bed coverage.
- The re-coating can effectively fill depressions from rough substrate surfaces.

GRAPHICAL ABSTRACT

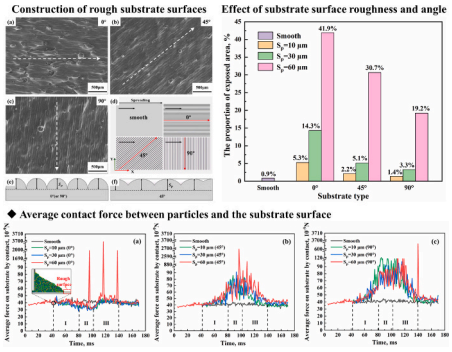

ARTICLE INFO

Keywords:
Discrete element method
Laser powder bed fusion
Powder spreading
Surface roughness
Surface texture

ABSTRACT

Controlling the quality of the powder bed is critical for guaranteeing component quality in laser powder bed fusion (LPBF). In this work, the discrete element method is used to examine how substrate surface morphology, including the roughness and texture angle, affects powder bed quality. The results indicate that the bed quality is more sensitive to changes in surface roughness than texture angle. Powder coverage can be improved by increasing the texture angle. The force analysis reveals that on rough surfaces, the contact force acting on the substrate has strong fluctuations. The particle-substrate contact force under the piles has an increasing-decreasing trend with the distance from the scraper increasing. In addition, the in-situ re-coating technique at a proper gap increment can effectively fill the depressions generated from the rough surface, achieving more uniform and dense powder beds. The findings provide a theoretical basis for optimizing powder-spreading strategies in LPBF process.

☆ This article is part of a Special issue entitled: 'CPT & CMGM 2024' published in Powder Technology.

* Corresponding author at: Jiangxi Provincial Key Laboratory of Particle Technology, Jiangxi University of Science and Technology, Nanchang 330013, China.
E-mail address: zongyan.zhou@jxust.edu.cn (Z. Zhou).

https://doi.org/10.1016/j.powtec.2025.121296
Received 5 December 2024; Received in revised form 17 June 2025; Accepted 19 June 2025
Available online 20 June 2025

1. Introduction

Laser Powder Bed Fusion (LPBF) technology is one of the most promising additive manufacturing technologies for producing complex metal components [1–3]. In the LPBF process, the metal powder is spread first onto the substrate by a scraper, and then the laser beam melts the metal powder layer by layer, thus building the three-dimensional parts [4,5]. The quality of the powder bed, including its density and surface roughness, influences the melting process and quality and mechanical properties of components [5]. Powder beds with poor quality can lead the uneven energy absorption and unstable melt pools, which increases the risk of defect generation [6]. A good quality of powder beds can achieve products with higher density and superior performance [7,8]. Therefore, improving the quality of the powder bed is one of the effective methods to guarantee product quality in LPBF.

The quality of powder beds is affected by many variables, which mainly include particle-related, operation-related, and substrate-related properties [9–11]. For example, the particle-related properties consist of size distribution [12,13], powder morphology [14–16], and adhesions [17]. The operation-related properties include powder spreading speed [18–20], layer thickness [19–21], and the shape of scrapers [22]. Many studies have been conducted to quantify the effects of these variables, either experimentally or numerically, particularly the application of the discrete element method (DEM) [23–25]. Generally, particles with a broad size distribution can achieve a high packing density [12], and the moderate adhesion induced by fine particles can improve the uniformity of the powder bed. However, the presence of a large quantity of fine particles leads to stronger adhesion between particles, which may reduce the packing density and surface smoothness of the powder bed [17]. The powder bed is also influenced by the powder sphericity [14] and experimental studies have shown that powder with higher sphericity can promote the densification of the powder bed, effectively reducing defects in the final components [15,16]. Higher spreading speed increases the surface roughness and decreases the packing density [18,19,21]. Increasing the layer thickness can enhance the final bed packing density [19–21], and also can reduce printing time, thus improving manufacturing efficiency [26]. For powder spreading tools, circular and inclined surface blades can deposit more particles than vertical blades [22], and improve powder deposition efficiency [27,28]. Larger roller diameters can increase powder bed density, and the roller speed has little effect [29].

In addition to the factors mentioned above, the surface morphology of the substrate is also one of the important factors. In many numerical studies, the substrate is generally assumed smooth; but in reality, the surface of the substrate is formed by the melt-solidified metal powders. Thus, the surface may exhibit balling and warping, caused by spattering and improper printing parameter settings [30]. Studies of Nan et al. [31,32] show that for a rough substrate composed of overlapping cylinders, with the layer thickness increasing, the exposed defect area and average defect length decrease. The degree of particle segregation by

Table 1
TC4 powder parameters used in the simulation.

Parameter	Value
Particle size, d	13–80 μm
Particle density, ρ	4430 kg/m^3
Coefficient of sliding friction, μ_s	0.3
Coefficient of rolling friction, μ_r	0.01
Young's modulus, Y	1.1×10^8 P$_a$
Coefficient of restitution, e	0.4
Poisson's ratio, ν	0.3
Hamaker constant, H	1.2×10^{-20} J
Time step	0.005 μs
Spreading speed	0.05 m/s
Layer gap	120 μm
Roughness, S_p	10 μm, 30 μm, 60 μm

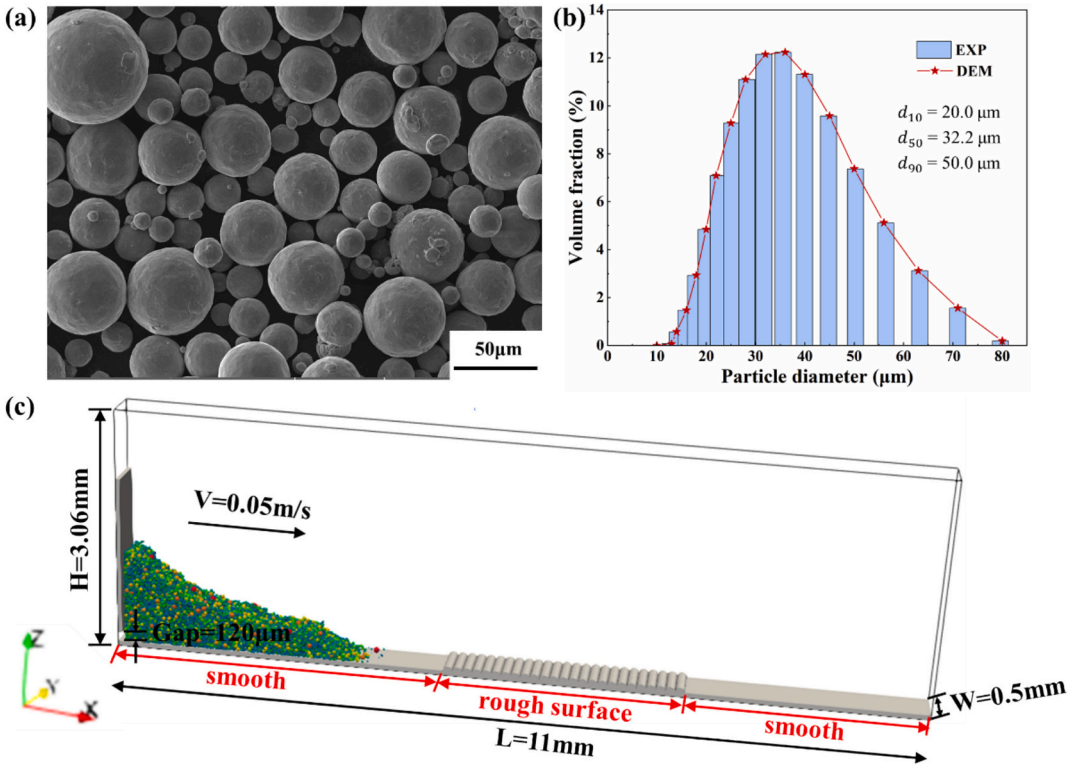

Fig. 1. TC4 alloy powder and powder spreading model: (a) actual powder morphology of TC4 powder, (b) comparison of particle size distribution between simulation and experiment, and (c) schematic diagram of the powder spreading model.

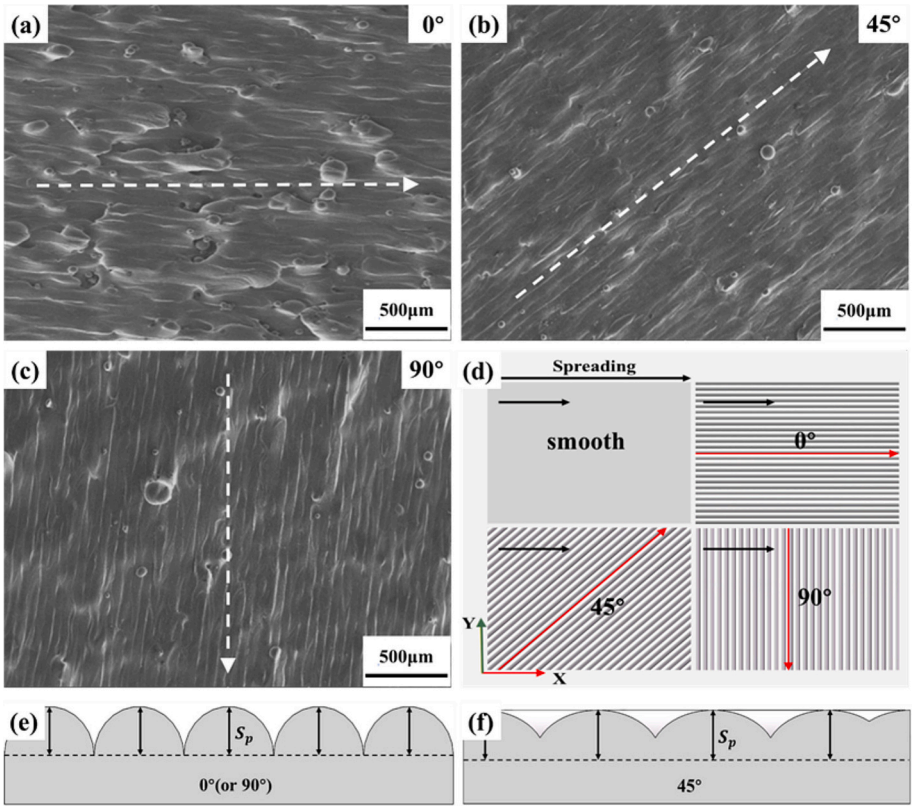

Fig. 2. Powder spreading strategies: (a), (b), and (c) are morphologies obtained under the different laser scanning directions; (d) shows the smooth surface substrate and rough surface substrates with different angles (0°, 45°, and 90°) designed in the simulation; (e) and (f) are schematic diagrams illustrating the definition of roughness at 0°, 45°, and 90° (front view).

diffusion decreases with increasing layer thickness or decreasing roller speed. Xu et al. [33] also used the rough cylindrical substrate and found that the powder spreadability is more sensitive to rolling friction than adhesion force when the substrate surface roughness is small. Marchais et al. [34] simulated the rough substrate surface by arranging discrete elements in a regular pattern, and the precise control of the roughness can be achieved by adjusting the diameters of the discrete elements. The results indicate that powder bed quality is similar across different frictions, with the adhesive force playing a crucial role. Lower powder spreading speeds can improve powder bed quality. In addition, Xiang et al. [35] employed the surface morphology model to create a rough substrate and found that the bed roughness and relative layer packing density increase with the increase of the substrate roughness and layer thickness. With increasing the powder spreading speed, the bed roughness tends to increase first and then decrease, and the relative packing density decreases. Furthermore, the recent studies of Phua et al. [36] and Cook et al. [37] on laser melting substrate confirmed that the particle size and shape have significant influences on the powder spreading and deposition. Better powder coverage can be achieved by using finer, single-sized, and highly adhesive particles.

It should be noted that the studies above ignored the impact of the substrate texture direction and the roughness induced by the printing scan strategy and the solidification process. Therefore, in this paper, several rough surface substrates with different texture directions are constructed. The DEM method is used to quantitatively analyze the interactions between the rough substrate surface and particles, and the dynamic behavior of particles under different roughness levels is explored in-depth. The goal is to provide evidence for a better understanding of the powder spreading process in the rough substrate and developing effective optimization strategies.

2. Model description

In the DEM [24], particles are treated as discrete individuals and the motion of each particle can be determined based on Newton's second law of motion, thus enabling to obtain the overall flow and dynamic behavior of particulate systems. DEM has been widely applied in various research fields [38]. In the DEM, the interaction forces between particles primarily include normal and tangential viscoelastic contact force, friction, and cohesive forces such as van der Waals force. The motion of particles is divided into translational and rotational components, which can be written as [39,40]:

$$m_i \frac{d\mathbf{v}_i}{dt} = \sum_{j=1}^{k_c} \left(\mathbf{f}_{c,ij} + \mathbf{f}_{d,ij} \right) + m_i \mathbf{g} \tag{1}$$

$$\mathbf{I}_i \frac{d\boldsymbol{\omega}_i}{dt} = \sum_{j=1}^{k_c} \left(\mathbf{M}_{t,ij} + \mathbf{M}_{r,ij} \right) \tag{2}$$

where $\mathbf{v}_i$ and $\boldsymbol{\omega}_i$ are translational and rotational velocities of the particle i respectively, and k_c is the number of particles in interaction with

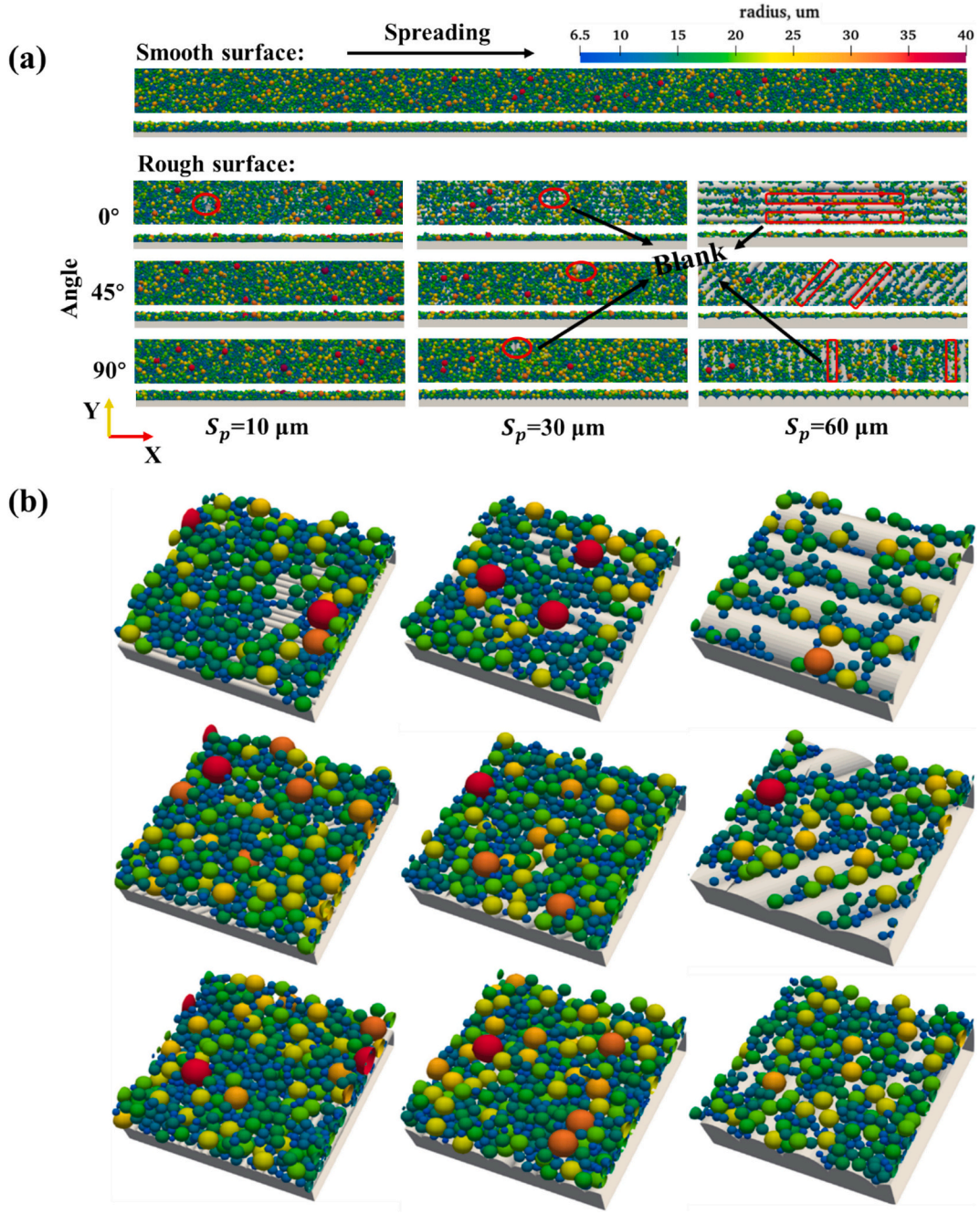

Fig. 3. (a) Top and side view morphologies of powder layers under different roughness and angle conditions; (b) the enlargement view of a specific region on various rough surfaces in the selected areas in (a).

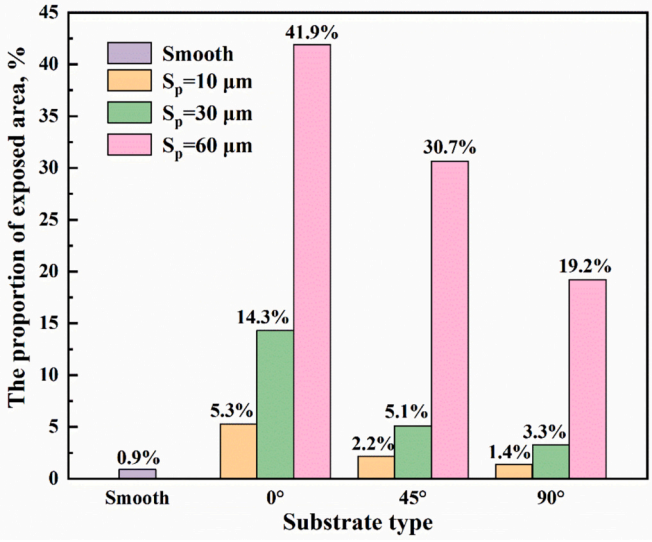

Fig. 4. Proportion of exposed area in the rough region of the substrate under different roughness and angle conditions.

particle *i*. The simulated forces involve particle gravity of $m_i\mathbf{g}$, and inter-particle forces between particles that include elastic contact force $\mathbf{f}_{c,ij}$, viscous damping force $\mathbf{f}_{d,ij}$. These contact forces between particles can be resolved into normal components and tangential components. The torque acting between particle *i* and particle *j* is divided into rotational torque ($\mathbf{M}_{t,ij}$) and rolling friction torque ($\mathbf{M}_{r,ij}$). $\mathbf{M}_{t,ij}$ is generated by tangential forces. That causes particle *i* to rotate, and $\mathbf{M}_{r,ij}$ is generated by rolling friction which opposes the relative rotation of particle *i*. The acceleration of the particles is governed by the interaction forces, while their rotation is determined by torques. By iteratively calculating these forces and motion states, DEM can effectively simulate the complex dynamic behavior of particulate systems.

The contact force between particles is typically described using the Hertz-Mindlin contact model [41–43], which divides the force into normal and tangential components to represent the elastic deformation and frictional behavior of the particles. First, the normal force model is based on Hertzian contact theory, which describes the force generated by elastic deformation during particle contact. For two elastic particles in contact, the normal force $\mathbf{f}_n$ has a nonlinear relationship with the normal overlap depth $\boldsymbol{\delta}_n$, and its calculation formula is as follows [42]:

$$\mathbf{f}_n = \frac{4}{3}E^*\sqrt{R^*}\boldsymbol{\delta}_n^{\frac{3}{2}} \tag{3}$$

where E^* is the effective Young's modulus, and R^* is the effective radius of the two contacting particles.

The tangential contact force is based on the Mindlin model, which describes the frictional interaction between particles. The relationship between the tangential force $\mathbf{f}_t$ and the tangential displacement $\boldsymbol{\delta}_t$ is given by [43]:

$$\mathbf{f}_t = 8G^*\sqrt{R^*\delta_n}\boldsymbol{\delta}_t \tag{4}$$

where G^* is the effective shear modulus.

The normal contact force also needs to account for the influence of adhesive forces between particles. In this work, the van der Waals force model based on Hamaker theory [44,45] is used. The van der Waals force is the inherent force between materials, and it is expressed by the following formula:

$$f_v = -\frac{H}{6}\left[\frac{2r_ir_j}{d^2-(r_i+r_j)^2}+\frac{2r_ir_j}{d^2-(r_i-r_j)^2}+ln\left(\frac{d^2-(r_i+r_j)^2}{d^2-(r_i-r_j)^2}\right)\right] \tag{5}$$

where H is the Hamaker constant, which determines the magnitude of the force, and d is the distance between the centers of particles i and j. When the distance exceeds 1 μm, the influence of the Van der Waals force is neglected in the simulation, as its effect becomes several orders of magnitude smaller than gravity.

3. Simulation conditions

The powder used in this study is the commercial Ti6Al4V (TC4) titanium alloy powder, and its morphology is shown in Fig. 1(a). As most powders used in LPBF are prepared by gas atomization with high sphericity, the particle shape is assumed spherical [46] in this work. A typical particle size distribution (PSD) of TC4 powder is shown in Fig. 1 (b), and the simulation uses a similar PSD. Fig. 1 (c) shows the schematic diagram of the powder spreading model used in this study. Note that the substrate is divided into two regions: smooth region and rough region. Periodic boundary conditions are applied in the Y-direction to eliminate wall effects. In this work, the open-source DEM software of LIGGGHTS is employed in simulation. The time step is set at 0.005 μs, and the powder spreading duration is 170 ms with the spreading distance of 11 mm. The computation time for each case is roughly 48 h with a single CPU core.

The DEM based on the LIGGGHTS has been used in our previous work [17], where the DEM parameters including friction coefficients and Hamaker constant were verified by the measured packing density and angle of repose. These DEM parameters are adopted in this work. The material properties of TC4 titanium alloy powder [17,47] are given in Table 1. The actual value of Young's modulus is 110 GPa, but to reduce computational time without affecting the simulation results, it is scaled down to 0.11 GPa. In the LPBF process, different scanning strategies can affect the surface texture and morphology of the manufactured parts, as shown in Figs. 2(a), (b), and (c). Based on the angle between the surface texture direction and the powder spreading direction, rough surface substrates with different angles (0°, 45°, and 90°) are constructed in this study, as shown in Fig. 2(d). The rough surface is represented by the parameter of S_p (Figs. 2(e) and (f)) based on the maximum peak height, while the smooth surface is used for the purpose of comparison.

4. Results and discussion

4.1. Effects of roughness and angle of texture on powder distribution

Fig. 3 (a) shows the top and side views of the powder layer formed after the spreading under different conditions. The results indicate that different-sized uncovered spots appear in the powder bed, where the major axis of spots closely corresponds to the angle of surface texture

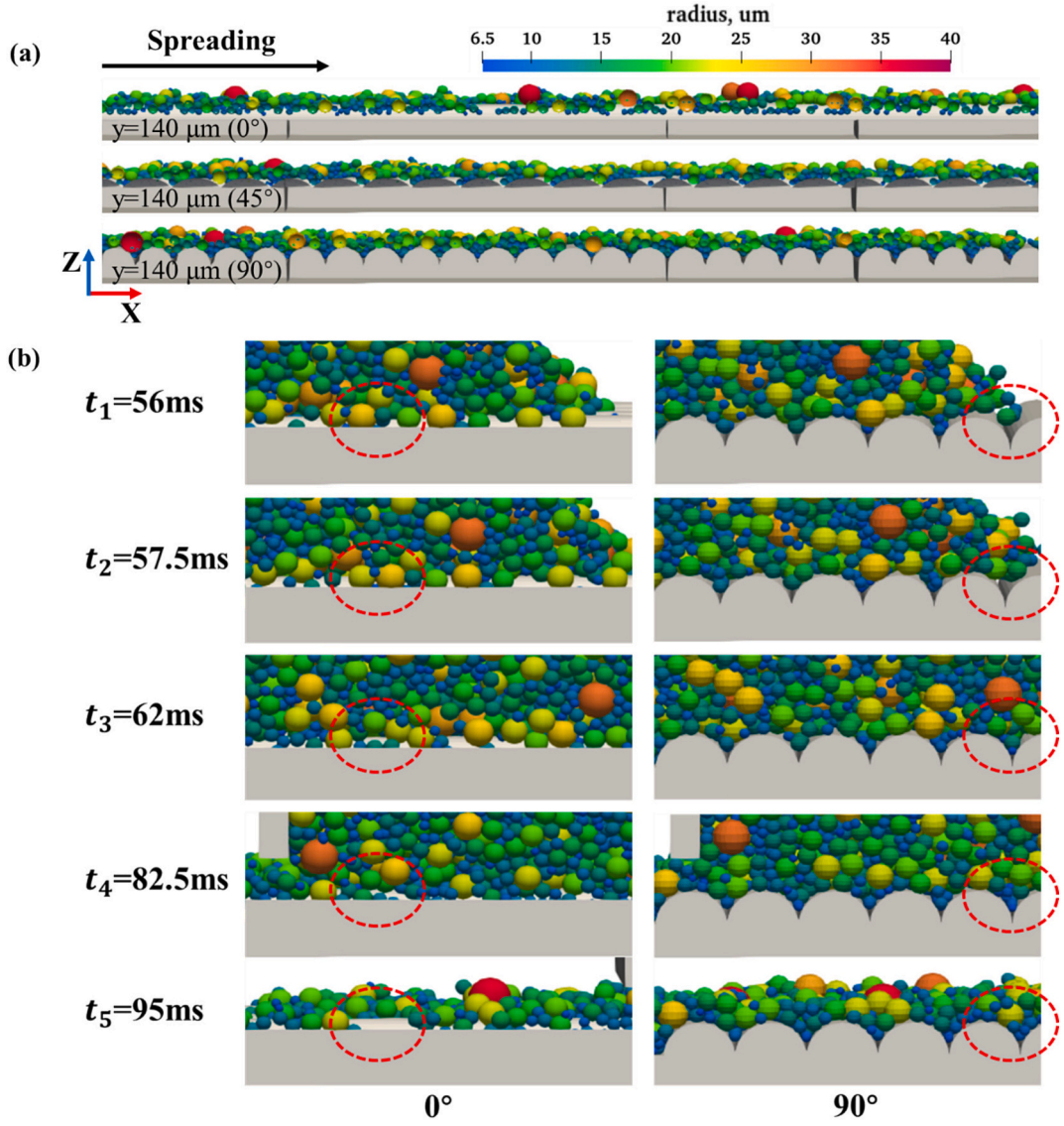

Fig. 5. (a) Front view of powder bed cross-sections along the y-axis at three different angles under high roughness conditions (S_p = 60 μm); (b) snapshots of specific areas at different times for 0° and 90°.

direction. With increasing the roughness (S_p), the powder coverage in the rough region decreases. Specifically, the reduction in powder coverage is particularly pronounced at the angle of 0° and S_p of 60 μm, exhibiting that the powder fails to completely cover the rough substrate. Particles tend to accumulate in the depression region, with only a few particles remaining on the elevated surfaces, as shown in Fig. 3(b). With the angle increasing, the movement of the particles can be hindered so that more particles remain on the substrate, thus making the quality of the powder bed effectively improved. To more clearly demonstrate the changes in powder coverage, the quantitative analysis of the proportion of exposed area in the rough regions is calculated and shown in Fig. 4. It can be observed that the surface roughness of S_p increases from 10 μm to 60 μm, the fraction of exposed area increases from 5.3 % to 41.9 % for the angle of 0°, 2.2 % to 30.7 % for the angle of 45°, and 1.4 % to 19.2 % for the angle of 90°. The data illustrate that both the surface roughness and the texture angle have significant effects on the exposed area. Furthermore, the powder coverage is more sensitive to changes in surface roughness than texture angle.

The longitudinal section view of powder beds (Fig. 5 (a)) is obtained along the powder spreading path (X-Z plane), showing the particle segregation in the vertical z-direction at different angles. This phenomenon is related to the texture direction of the substrate surface, exhibiting more depositions of small particles in the depression region at the angle of 90°, followed by the angle of 45° and 0°. At the angle of 90°, the surface texture is perpendicular to the powder spreading direction, making it difficult for large particles to roll and slide along the texture. Therefore, the large particles stay on the higher parts of the surface and do not easily fall into the depression region. In contrast, small particles are more easily trapped in depression regions and gradually fill the voids in the region. In comparison, at the angle of 0°, the surface texture is parallel to the powder spreading direction, which offers the least obstruction to particle movement. Large particles move more easily

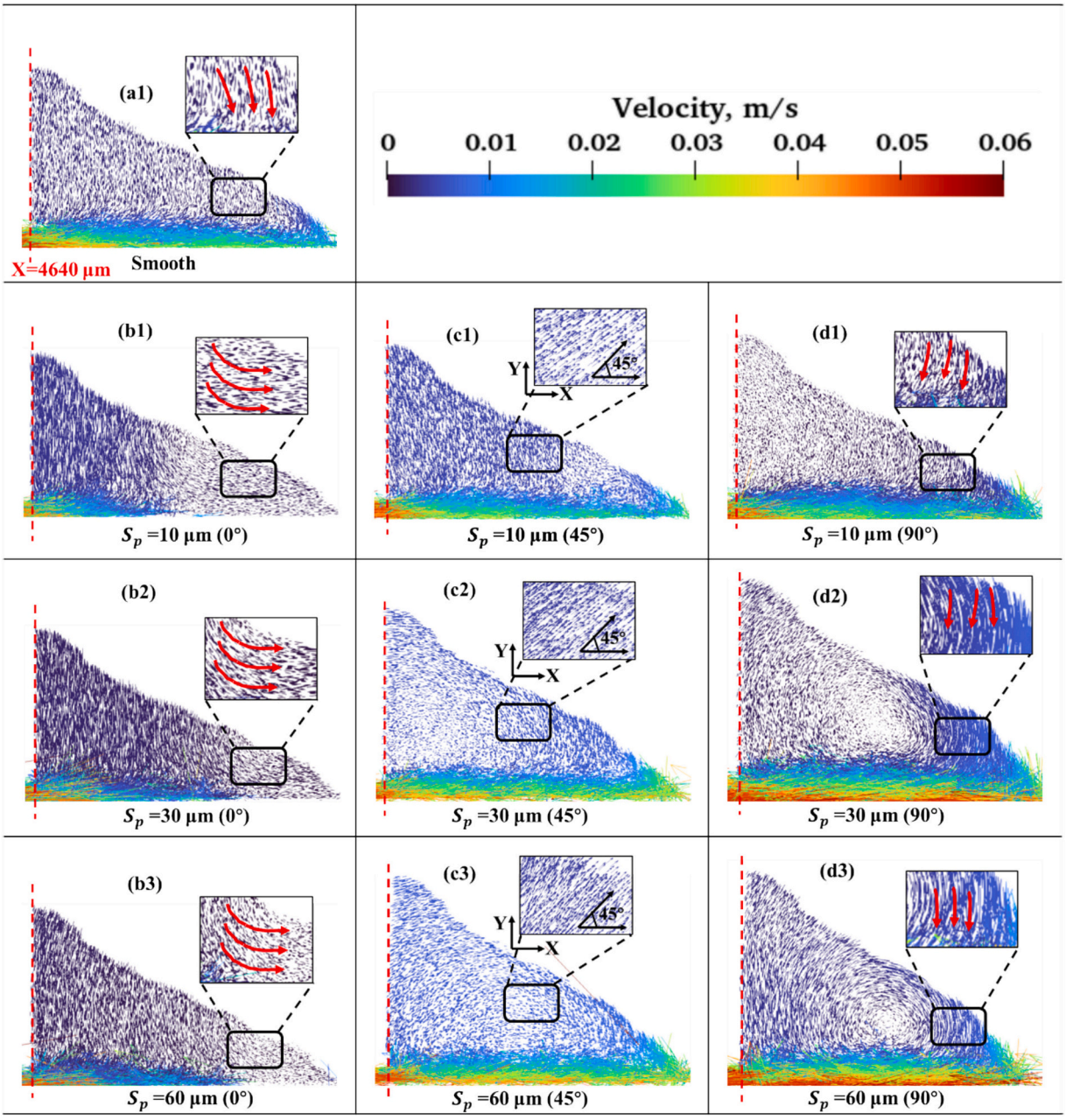

Fig. 6. Particle velocity vector distribution at $t = 93.8$ ms and x = 4640 μm during powder spreading under different conditions: (a1) Smooth; (b1) ~ (b3) 0°; (c1) ~ (c3) 45°; (d1) ~ (d3) 90°. Note that the velocities presented are relative velocities to the scraper speed, and the vector length is proportional to the velocity magnitude.

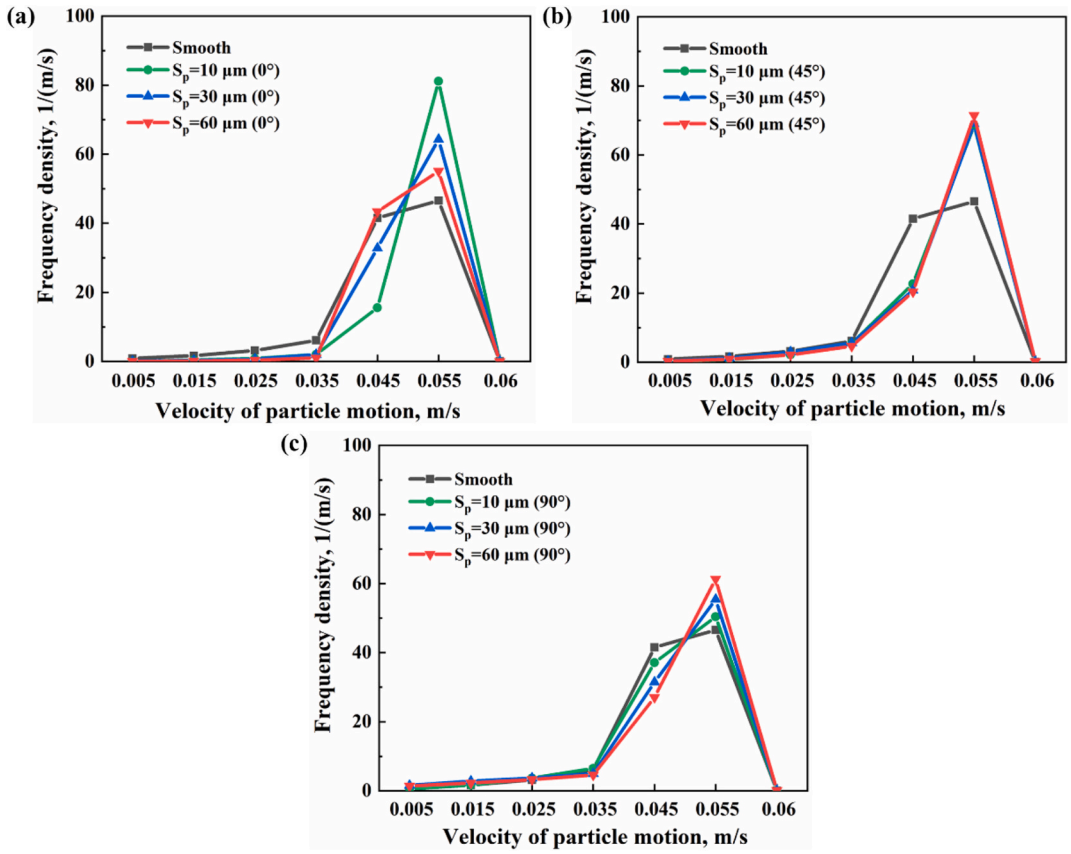

Fig. 7. Particle velocity distribution under different roughness and angles: (a) angle of 0°, (b) angle of 45°, and (c) angle of 90°.

along the surface, which results in fewer small particles being deposited into depression regions (Fig. 5 (b)).

4.2. *Effects of surface morphology on particle velocity*

The velocity vector distribution of particles under different roughness and surface texture conditions is shown in Fig. 6. To visually demonstrate the relative motions of particles under different conditions, the relative velocity is calculated as the velocity vector of the particle minus the spreader moving speed in the powder spreading direction [27]. It is worth noting that the relative movements of particles are very closely related to the surface texture conditions (Fig. 6). In the case of the angle of 0°, only the particles in the gap area in rear of the powder piles move backward while the particles in front of the piles move forward (Figs. 6(b1) ~ (b3)). This could be attributed to the unevenness of the surface substrate where the texture direction is aligned with the powder spreading direction. This causes the front part of the pile to sink and move forward. With the angle increasing, the movement direction of the particles tends to align with the angle of 45°, while the particles exhibit the circulating motion at the angle of 90°. The particles at the front of the pile exhibit a down-forward motion path, while the remaining particles move upward at low speed at the rear of the piles, forming a circulating motion. The circulation helps redistribute the particles on the rough surface, resulting in a relatively uniform and dense powder layer.

Figure 7 further shows the frequency distribution of particle velocity under different conditions, indicating that rough surfaces have a larger velocity than smooth surfaces. This is because rough surfaces can induce local disturbances in the particle flow, leading to greater velocity variations. This phenomenon means that some of the particles move at a higher velocity, leading to uneven distribution of particles in the powder spreading process, which is ultimately manifested in an increased percentage of bare area. In addition, rough surfaces increase the frequency and intensity of collisions between particles, changing their motion trajectories. However, the effect of rough surfaces on the velocity varies with the roughness and angles. For example, the peak of the particle velocity distribution decreases as roughness increases at the angle of 0° but the opposite trend is observed at the angle of 90°. At the angle of 0°, the increase in roughness makes particles more likely to accumulate in the depression regions of the surface, which reduces their overall movement speed (Fig. 7(a)). At the angle of 45°, the direction of motion of the particles is mainly influenced by the surface texture, and the increase in roughness does not significantly change the main motion mode of the particles. Therefore, the overall distribution of the curves does not change significantly despite the increase in roughness from 10 μm to 60 μm (Fig. 7(b)). However, increased roughness at the angle of 90° leads to more vertical contacts or collisions between the particles and the surface texture (Fig. 7(c)). As particles cross peaks and valleys, they experience changes in potential energy due to the height differences during the powder spreading process. When particles slide from the peak down to the valley, the potential energy is converted into kinetic energy, thereby increasing the relative velocity. With the roughness increasing, the

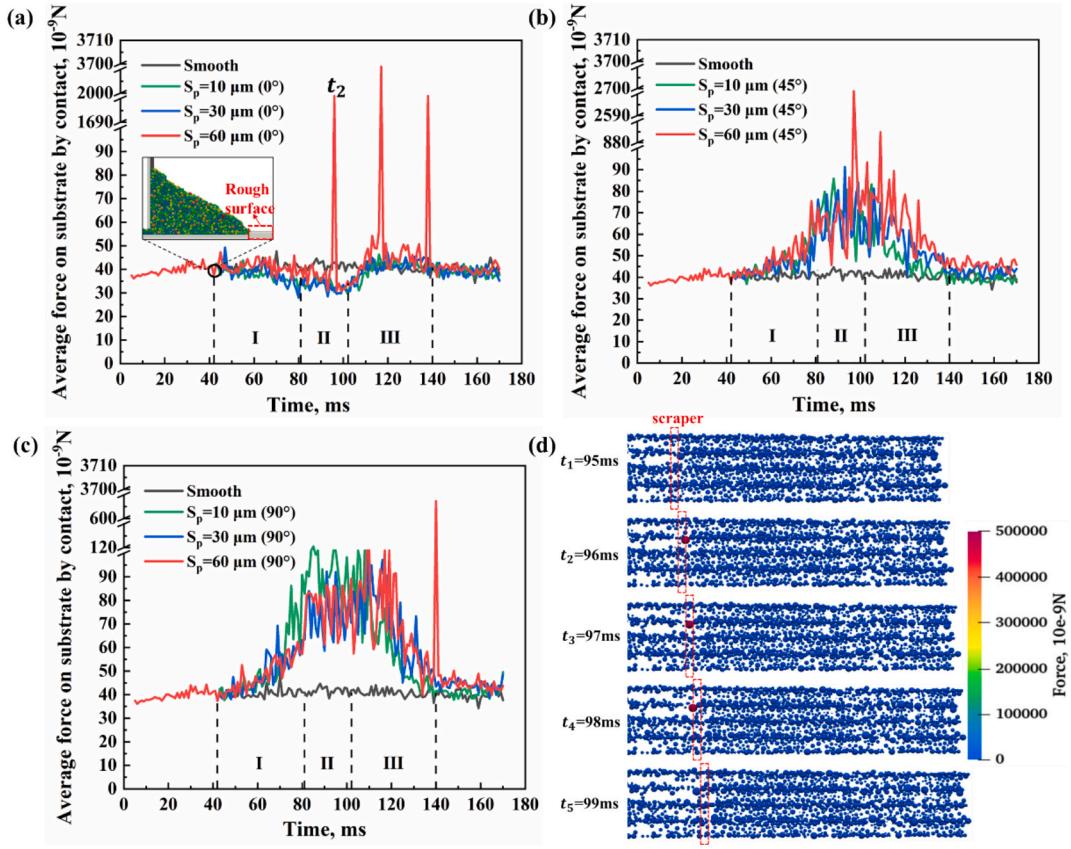

Fig. 8. Average contact force between particles and the substrate surface: (a) angle of 0°, (b) angle of 45°, (c) angle of 90°; (d) particle-substrate contact force distribution to explain the force peak shown in (a) at the time of $t_2 = 96$ ms. In the figures, I: 42 ms ~ 81 ms, powder pile in smooth and rough areas; II: 81 ms ~ 102 ms, powder pile completely in rough area; III: 102 ms ~ 140 ms, powder pile in smooth and rough areas. Note that when calculating the average contact force in (a) ~ (c), the calculation domain starts from the right plane of the scraper.

potential-to-kinetic energy conversion effect becomes more pronounced, resulting in higher particle velocities.

4.3. Effects of surface morphology on particle dynamics

4.3.1. Interaction forces between particles and substrate

During the powder spreading, the interaction forces between particles and the substrate directly influence the stability of particles on the substrate. Figs. 8 (a) ~ (c) shows such interactions under different roughness and angle conditions. Taking $S_p = 60$ μm at the angle of 0° as an example (Fig. 8(a)), the front of the powder piles starts to contact the rough region at 42 ms (see the inset), where the contact force between the particles and the substrate starts to change. In region I (42 ms ~ 81 ms), the powder pile is partly on the smooth surface and partly on the rough surface. In the case of 0°, the average contact force between the particles and the rough surface tends to decrease compared with that of the smooth surface; while the cases of 45° and 90° show an increase. This is because the surface texture at 0° is in the same direction as the powder spreading direction, and the particles can slide smoothly and the contact area with the substrate surface is smaller than that of the smooth surface. With the surface texture at 90°, the particles will frequently come into perpendicular contact, increasing the contact force. With the surface texture at 45°, the particles can slide along the rough surface at a certain angle in which the increase in contact force is not as obvious as that at 90°. In region II (81 ms ~ 102 ms), the whole powder pile is completely on the rough surface, so the contact force tends to be stable regardless of 0°, 45°, or 90°. When the powder pile starts to leave the rough region into the smooth region (region III: 102 ms ~ 140 ms), the average contact force between the particles and the substrate in the cases of 0°, 45°, and 90° shows the opposite trend from that in the region I. Generally, the fluctuations in the average contact force between particles and the substrate are large at angles of 45° and 90°, compared to that of the case of 0°. It can also be seen from Figs. 8 (a) ~ (c) that the average contact force between the particles and the substrate is not sensitive to roughness, and that the texture angle leads to a more complex motion of the particles as they move across the surface.

It should be noted that at 45° and 90°, the surface texture can hinder particles movement, leading to larger fluctuations in the contact force between the particles and the substrate. Moreover, extremely large forces occasionally occur at specific moments within the rough region for all angles with the S_p value of 60 μm. The large forces mainly exert on large particles, and an illustration is shown in Fig. 8(d). After entering the rough region, some large particles may experience retention or jamming on the raised surface structures, causing significant internal compression and pushing forces between particles. This close interaction results in a rapid increase in contact force over a short period, forming large force peaks.

The piles can be evenly divided into five sections for further analysis

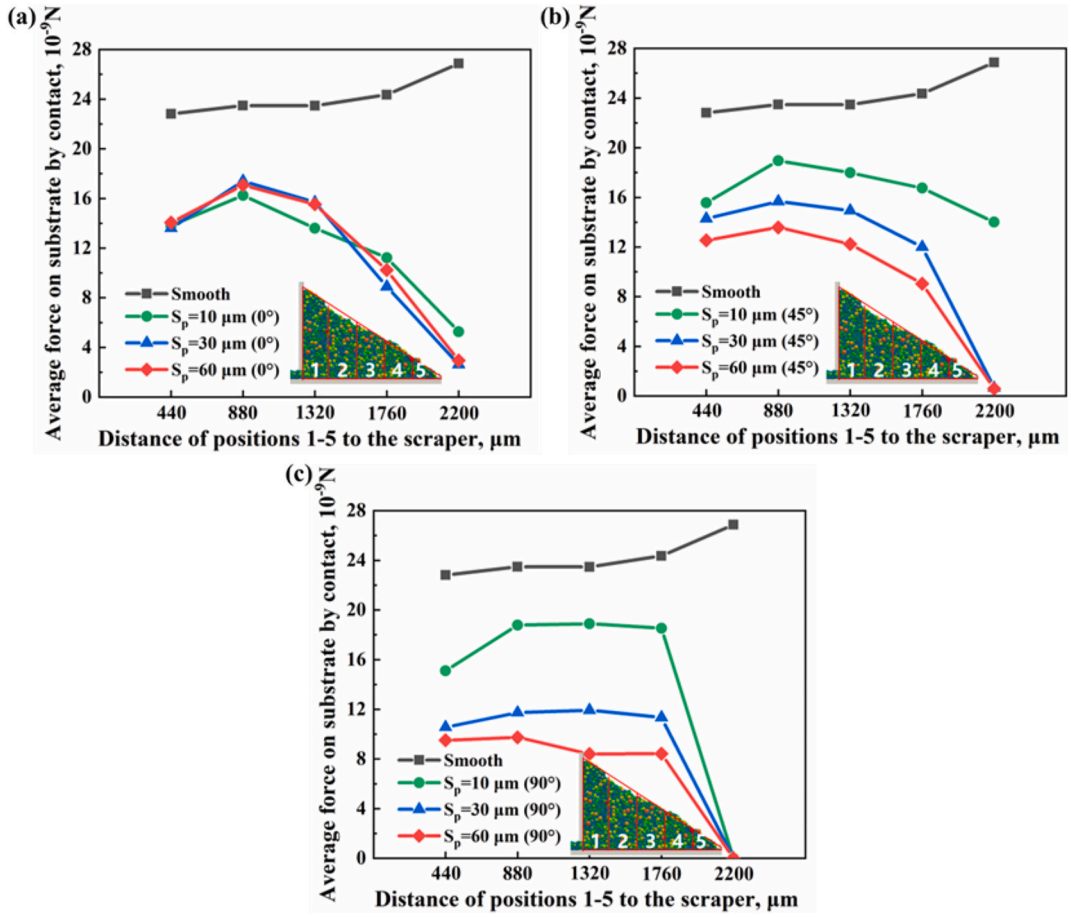

Fig. 9. Distribution of average contact force between particles and the substrate surface: (a) angle of 0°; (b) angle of 45°; (c) angle of 90°.

of particle-substrate interactions (see the inset in Fig. 9, but note that each section, e.g., positions 1–5, has fixed distance to the scraper, varying from 440 μm to 2200 μm). It can be observed that on the rough surface, with the distance to the scraper increasing, the force increases first and decreases, showing that particles farther away from the scraper have slightly higher contact force than particles closer to the scraper. This is largely because the particles at positions 2–4 can have downward motions as shown in Fig. 6, which leads to stronger particle-substrate interaction. Position 5 is located at the front tail region of the pile, which has less number of particles and hence, the corresponding force is weaker. On the smooth surface (here, the smooth surface is the first part of the spreading distance, see Fig. 1), the average contact force between particles and substrate shows little variation from positions 1 to 3, and then becomes higher at positions 4 and 5. This is because the pile size on the smooth surface is larger than that on the rough surface. Thus, the positions 4 or 5 of piles on the smooth surfaces are not located in the pile tail region. They are experiencing stronger particle-substrate interactions, causing slightly larger contact force shown in Fig. 9.

Figure 9 also indicates the effect of the angle and roughness on the particle-substrate contact forces. For example, the smooth substrate has the strongest contact forces. With the roughness increasing, the contact force decreases significantly, particularly at the angles of 45° and 90° (see Figs. 9 (b) and (c)). This is closely related to the occurrence of the size-induced segregation (see Figs. 3 and 5). With the roughness increasing, more small particles can percolate to the valley, and the contact force of small particles is much smaller than large particles, causing the decreased contact force. It should be mentioned that the angle also plays a significant role. Large angles will make small particles easily settle down in the valley and percolate to the bottom. Thus, the contact force becomes smaller. This is particularly true when the roughness is large (for example, at 30 μm and 60 μm).

4.3.2. *Interaction forces between particles and the scraper*

In the LPBF process, the scraper spreads powder onto the build platform, directly influencing the quality of the powder bed. Fig. 10 shows the average contact force between the particles and the scraper under different roughness and angle conditions. It can be observed that the greater the roughness, the larger the fluctuations in the force exerted on the scraper. Meanwhile, the magnitude of the contact force increases with the roughness increasing. In particular, at S_p = 60 μm, the force exerted by the scraper increases significantly at certain moments due to the reduced gap between the scraper and the substrate surface. In addition, larger particles splashing can be distinguished, attributing to colliding with the scraper at the angle of 45° and 90° and high roughness during the spreading (Fig. 10 (d)). Larger particles entering this region experience friction with the scraper and may even be compressed. This friction and compression effect causes the scraper to apply greater force to overcome resistance, leading to a sudden increase in contact force.

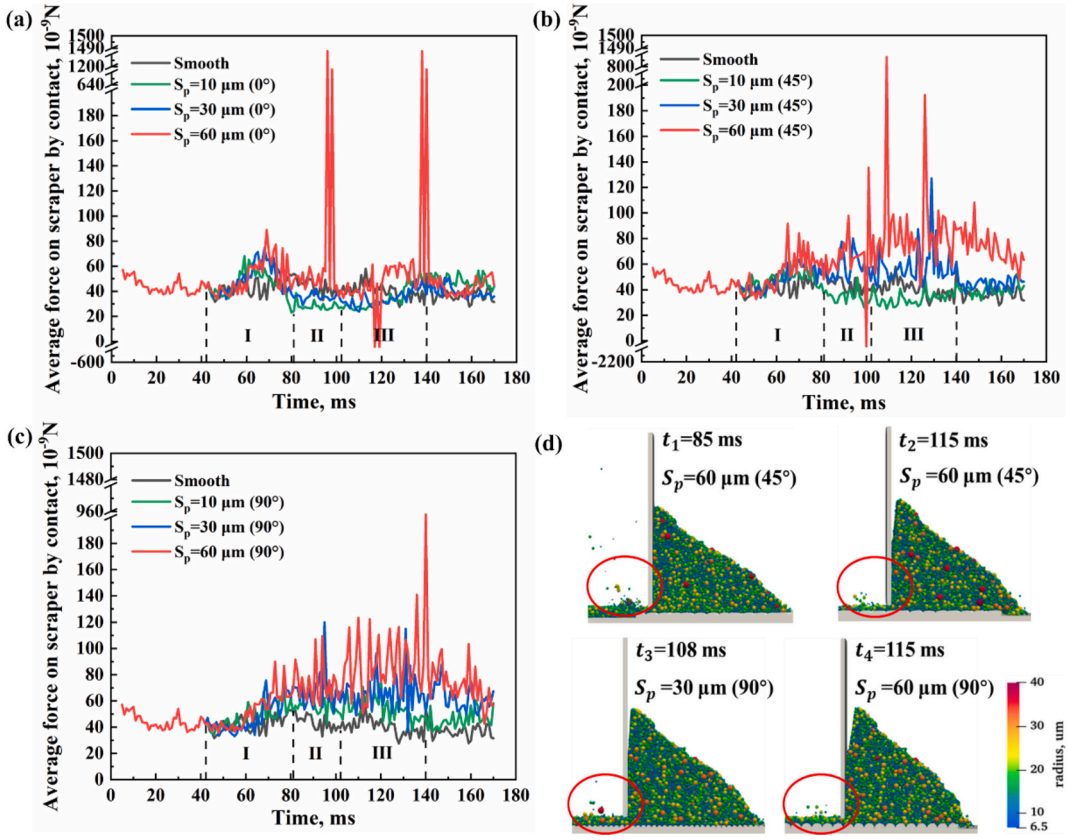

Fig. 10. Average contact force between particles and the scraper surface: (a) angle of 0°; (b) angle of 45°; (c) angle of 90°; (d) particle splashing. (I: 42 ms ~ 81 ms, powder pile in smooth and rough areas; II: 81 ms ~ 102 ms, powder pile completely in rough area; III: 102 ms ~ 140 ms, powder pile in smooth and rough areas).

4.3.3. *Inter-particle interaction forces*

During the powder spreading, the particles in the piles are influenced by gravity, internal friction forces, and adhesion forces, generating complex force chains. As observed in Fig. 11, the strongest force chains are mainly concentrated in the gap area in front of the scraper. These force chains dynamically change as the particles move, causing the average force to fluctuate continuously. With the roughness of the substrate surface increasing, the strength of the force chains also increases. Moreover, under the same roughness conditions, the strength of the contact force chains increases as the angle between the substrate surface texture and the powder spreading direction increases.

To further quantify the changes in forces between particles, Fig. 12 presents the variation curves of the average contact force between particles under different roughness and angle conditions. As the substrate surface roughness and the angle increase, the average contact force between particles increases from 23.6 nN to 28.1 nN at the angle of 0°, 28.6 nN to 37.3 nN at the angle of 45°, and 30.2 nN to 42.9 nN at the angle of 90°, respectively. The particles slide parallel to the surface texture at the angle of 0° and encounter less obstruction from the substrate, which results in relatively lower contact forces between the particles. Hence, the effect of the roughness is not much. However, as the angle increases, the particles interact more frequently with the protrusions and depressions of surface texture, leading to greater friction and resistance.

4.4. *Simulation of powder recoating in depressed areas*

During the LPBF process, discontinuities in the material are created in some of the scanned areas due to insufficient powder, which leads to incomplete fusion of the layers, further exacerbated by thermal stresses within the part [30]. In this work, the roughness of the substrate surface leads to incomplete powder coverage (Fig. 3), which can also lead to lack of fusion defects of the parts during subsequent fabrication. To address this issue, we propose an in-situ re-coating method (Fig. 13 (a)), which can make real-time corrections by increasing the gap over the exposed rough areas. In this work, the in-situ recoating process is tested in the case of 0° as it has the largest proportion of exposed area.

Figure 13 (b) shows the effect of the gap increment on the powder bed. As observed, the depression region can be effectively filled by increasing the gap of the rough region by an appropriate amount. In order to show this effect more clearly, a certain area (red box region) in Fig. 13 (b) is selected and enlarged, as shown in Fig. 14 (a). To further confirm, the red line area in Fig. 13 (b) was intercepted along the y-direction, and the distribution of large and small particles in the z-direction is shown in Fig. 14 (b). It is obvious to see that more small particles are located in the lowermost layer. The proper gap increment can indeed make the powder bed height nearly level with the smooth surface areas (Fig. 13 (b)). But note that when the gap is too large (e.g., at 60 μm as shown in Fig. 13 (b)), the powder bed formed in the rough area will be much thicker than the bed in smooth areas. This will

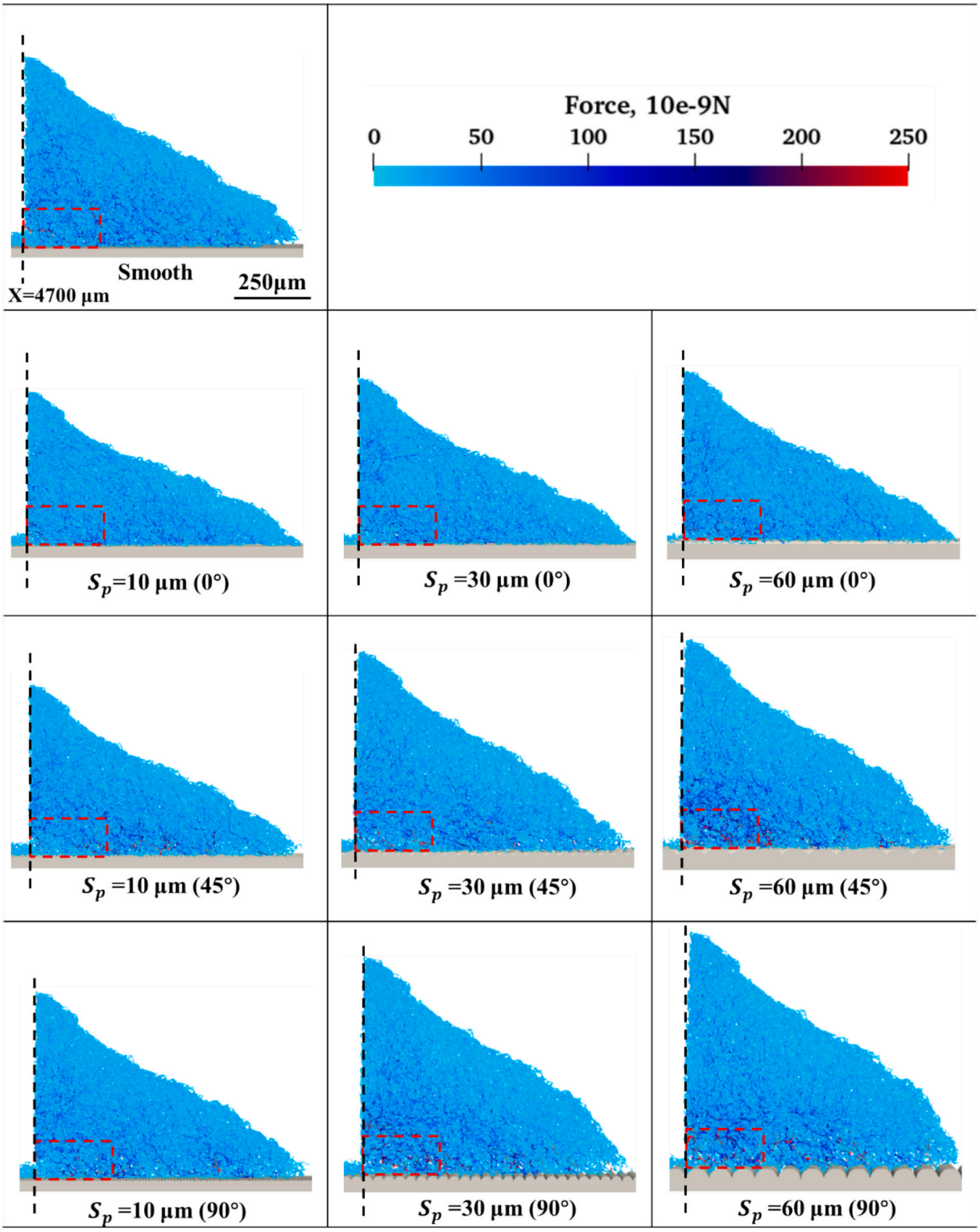

Fig. 11. Force chains between particles at t = 95 ms and x = 4700 μm under different roughness and angle conditions. (The red box is the area for calculating the average contact force between particles, which is 500 μm in length and 250 μm in width.) (For interpretation of the references to colour in this figure legend, the reader is referred to the web version of this article.)

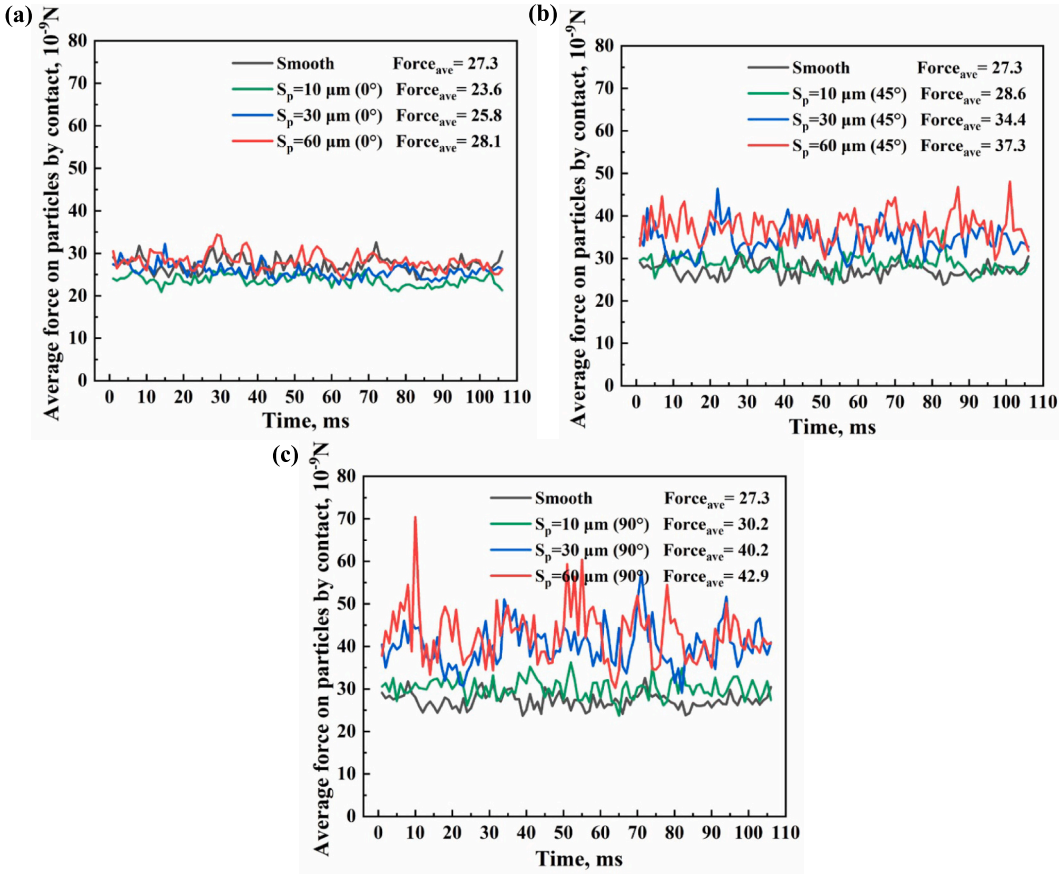

Fig. 12. Average contact force between particles: (a) angle of 0°; (b) angle of 45°; (c) angle of 90°.

generate issues such as the shortage of laser energy and then the formation of more defects. Hence, although the in-situ recoating method can improve the powder bed quality, the proper magnitude of the gap increment should be carefully determined. From the simulation results, the gap increment of 20–30 μm should be a reasonable selection.

5. Conclusions

The DEM method is used in this work to simulate the powder spreading process in laser powder bed fusion, focusing on the effect of the roughness of the substrate and the texture angles on the bed quality. The roughness and texture of the surface are implemented according to the maximum peak height (S_p) and the angle (0°, 45°, 90°) between the surface texture and powder spreading direction, respectively. The following conclusion can be drawn:

- The proportion of exposed area significantly increases from 5.3 % to 41.9 % with the increase in roughness from 10 μm to 60 μm at the angle of 0°, leading to numerous void defects in the forming area. This phenomenon can be mitigated by changing the angle to 90°, in which the worst proportion is 19.2 % in the roughness of 60 μm.
- The roughness and angle of the surface texture have a significant influence on particle velocity distribution, exhibiting significantly increased peak velocity compared to the smooth surface texture. The increase in roughness results in greater hindrance and directional changes for the particles during movement, especially at angles of 45° and 90°.
- The contact force on rough surfaces exhibits an increasing-decreasing trend with the distance from the scraper increasing, attributing to the particle downward motions in the pile and also less contacts in the pile tail region. The average contact forces between particles and rough surfaces are more unstable, with strong fluctuations. The average contact force between particles increases with increasing the roughness and angle of the surface texture.
- The in-situ re-coating technique is tested to enhance the uniformity and density of the powder bed, which can fill the uncovered area caused by the roughness of the substrate surface. However, the adjustment of the layer gap in the in-situ re-coating process must be moderated. Otherwise, excessive powder thickness might be generated and then the laser energy will be insufficient, resulting in an increase in internal defects and affecting the mechanical strength of components.

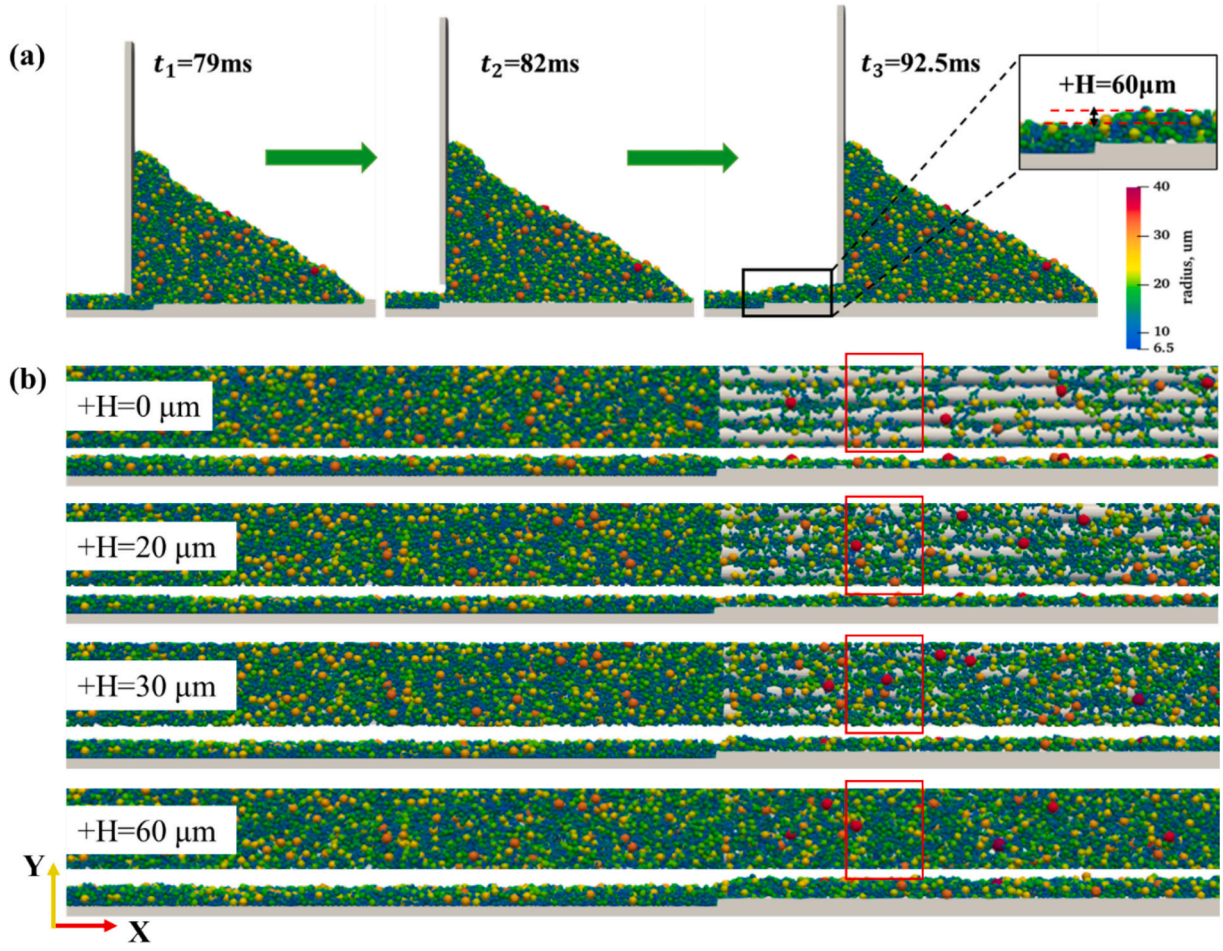

Fig. 13. (a) In-situ recoating process; (b) Top and side views of the powder bed in the rough area under different gap increment values.

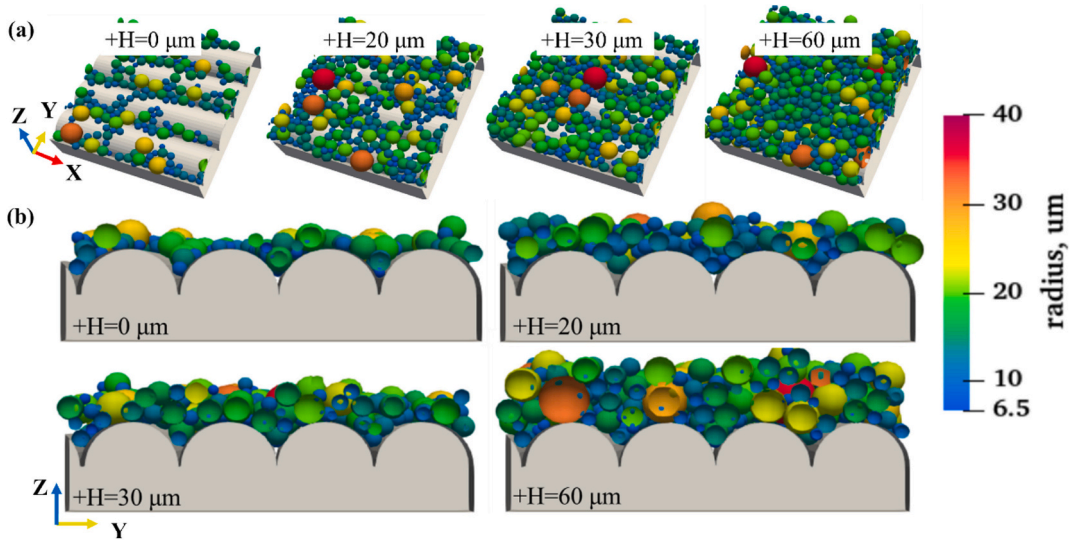

Fig. 14. Enlarged view of the red boxed area in Figure 13 (b): (a) three-dimensional view; (b) side view. (For interpretation of the references to colour in this figure legend, the reader is referred to the web version of this article.)

CRediT authorship contribution statement

Yaping Wu: Writing – original draft, Visualization, Validation, Software, Methodology, Investigation, Formal analysis, Data curation. **Fuzhong Chu:** Writing – review & editing, Visualization, Validation, Investigation, Data curation, Conceptualization. **Chaocai Zhang:** Writing – review & editing, Visualization, Validation, Investigation. **Hongyu Yan:** Writing – review & editing, Visualization, Validation, Investigation. **Lin Wang:** Writing – review & editing, Visualization, Validation, Software, Resources, Investigation. **Zongyan Zhou:** Writing

– review & editing, Visualization, Validation, Supervision, Software, Resources, Project administration, Methodology, Investigation, Funding acquisition, Formal analysis, Data curation, Conceptualization.

Declaration of competing interest

The authors declare that they have no known competing financial interests or personal relationships that could have appeared to influence the work reported in this paper.

Acknowledgement

The authors are grateful for the financial support for this work from the National Natural Science Foundations of China (52276154).

Data availability

Data will be made available on request.

References

[1] L.E. Murr, S.M. Gaytan, D.A. Ramirez, E. Martinez, J. Hernandez, K.N. Amato, P. W. Shindo, F.R. Medina, R.B. Wicker, Metal fabrication by additive manufacturing using laser and Electron beam melting technologies, J. Mater. Sci. Technol. 28 (2012) 1–14.
[2] C. Zhao, B. Shi, S.L. Chen, D. Du, T. Sun, B.J. Simonds, K. Fezzaa, A.D. Rollett, Laser melting modes in metal powder bed fusion additive manufacturing, Rev. Mod. Phys. 94 (2022) 045002.
[3] F.Z. Chu, H.P. Shen, J.W. Liu, J. Hou, K. Zhang, Z.Y. Zhou, Y.M. Zhu, X.H. Wu, A. J. Huang, Improved ductility by reducing powder size in laser powder bed fusion of AlSi10Mg, AMF 3 (2024) 200122.
[4] T. DebRoy, H.L. Wei, J.S. Zuback, T. Mukherjee, J.W. Elmer, J.O. Milewski, A. M. Beese, A. Wilson-Heid, A. De, W. Zhang, Additive manufacturing of metallic components – process, structure and properties, Prog. Mater. Sci. 92 (2018) 112–224.
[5] C.Y. Yap, C.K. Chua, Z.L. Dong, Z.H. Liu, D.Q. Zhang, L.E. Loh, S.L. Sing, Review of selective laser melting: materials and applications, Appl. Phys. Rev. 2 (2015) 041101.
[6] S.A. Khairallah, A.T. Anderson, A. Rubenchik, W.E. King, Laser powder-bed fusion additive manufacturing: physics of complex melt flow and formation mechanisms of pores, spatter, and denudation zones, Acta Mater. 108 (2016) 36–45.
[7] P.K. Gokuldoss, S. Kolla, J. Eckert, Additive manufacturing processes: selective laser melting, electron beam melting and binder jetting—selection guidelines, Mater 10 (2017) 672.
[8] S. Berumen, F. Bechmann, S. Lindner, J.-P. Kruth, T. Craeghs, Quality control of laser- and powder bed-based additive manufacturing (AM) technologies, Phys. Procedia 5 (2010) 617–622.
[9] L.C. Cao, J.C. Li, J.X. Hu, H.P. Liu, Y.D. Wu, Q. Zhou, Optimization of surface roughness and dimensional accuracy in LPBF additive manufacturing, Opt. Laser Technol. 142 (2021) 107246.
[10] G.X. Miao, W.C. Du, Z.J. Pei, C. Ma, A literature review on powder spreading in additive manufacturing, Addit. Manuf. 58 (2022) 103029.
[11] H. Salehi, J. Cummins, E. Gallino, V. Garg, T. Deng, A. Hassanpour, M. Bradley, Optimising spread-layer quality in powder additive manufacturing: assessing packing fraction and segregation tendency, Processes 11 (2023) 2276.
[12] Y.F. Zhao, Y. Koizumi, K. Aoyagi, K. Yamanaka, A. Chiba, Characterization of powder bed generation in electron beam additive manufacturing by discrete element method (DEM), Mater. Today Proc. 4 (2017) 11437–11440.
[13] E.J.R. Parteli, T. Pöschel, Particle-based simulation of powder application in additive manufacturing, Powder Technol. 288 (2016) 96–102.
[14] S.K. Yim, H.K. Bian, K. Aoyagi, K. Yamanaka, A. Chiba, Spreading behavior of Ti48Al2Cr2Nb powders in powder bed fusion additive manufacturing process: experimental and discrete element method study, Addit. Manuf. 49 (2022) 102489.
[15] S.E. Brika, L. Morgan, C.A. Dion, V. Brailovski, Influence of particle morphology and size distribution on the powder flowability and laser powder bed fusion manufacturability of Ti-6Al-4V alloy, Addit. Manuf. 31 (2020) 100929.
[16] F.Z. Chu, K. Zhang, H.P. Shen, M.J. Liu, W.J. Huang, X. Zhang, E.Q. Liang, Z. Y. Zhou, L.M. Lei, J. Hou, A.J. Huang, Influence of satellite and agglomeration of powder on the processability of AlSi10Mg powder in laser powder bed fusion, J. Mater. Res. Technol. 11 (2021) 2059–2073.
[17] L. Wang, E.L. Li, H. Shen, R.P. Zou, A.B. Yu, Z.Y. Zhou, Adhesion effects on spreading of metal powders in selective laser melting, Powder Technol. 363 (2020) 602–610.
[18] S. Haeri, Y. Wang, O. Ghita, J. Sun, Discrete element simulation and experimental study of powder spreading process in additive manufacturing, Powder Technol. 306 (2017) 45–54.
[19] Y.M. Fouda, A.E. Bayly, A DEM study of powder spreading in additive layer manufacturing, Granul. Matter 22 (2019) 10.
[20] H. Chen, T. Cheng, Z.W. Li, Q.S. Wei, W.T. Yan, Is high-speed powder spreading really unfavourable for the part quality of laser powder bed fusion additive manufacturing? Acta Mater. 231 (2022) 117901.
[21] D.Z. Yao, X.Z. An, H.T. Fu, H. Zhang, X.H. Yang, Q.C. Zou, K.J. Dong, Dynamic investigation on the powder spreading during selective laser melting additive manufacturing, Addit. Manuf. 37 (2021) 101707.
[22] L. Wang, A.B. Yu, E.L. Li, H.P. Shen, Z.Y. Zhou, Effects of spreader geometry on powder spreading process in powder bed additive manufacturing, Powder Technol. 384 (2021) 211–222.
[23] E.J.R. Parteli, DEM simulation of particles of complex shapes using the multisphere method: application for additive manufacturing, AIP Conf. Proc. 1542 (2013) 185–188.
[24] P.A. Cundall, O.D.L. Strack, A discrete numerical model for granular assemblies, Geotechnique 29 (1979) 47–65.
[25] P.W. Cleary, Large scale industrial DEM modelling, Eng. Comput. 21 (2004) 169–204.
[26] H. Zhang, L.C. Zhang, H.Y. Liu, X.D. Niu, M.C. Lam, W.Z. Zhang, X.J. Jin, F.Z. Chu, X.H. Wu, S. Cao, Strong and ductile Al–Mn–mg–Sc–Zr alloy achieved in fabrication-rate enhanced laser powder bed fusion, Virtual Phys. Prototyp. 18 (2023) e2250769.
[27] L. Wang, Z.Y. Zhou, E.L. Li, H.P. Shen, A.B. Yu, Powder deposition mechanism during powder spreading with different spreader geometries in powder bed fusion additive manufacturing, Powder Technol. 395 (2022) 802–810.
[28] S. Haeri, Optimisation of blade type spreaders for powder bed preparation in additive manufacturing using DEM simulations, Powder Technol. 321 (2017) 94–104.
[29] J.T. Zhang, Y.Q. Tan, T. Bao, Y.L. Xu, X.W. Xiao, S.Q. Jiang, Discrete element simulation of the effect of roller-spreading parameters on powder-bed density in additive manufacturing, Mater 13 (2020) 2285.
[30] M. Kuntoğlu, E. Salur, E. Canli, A. Aslan, M.K. Gupta, S. Waqar, G.M. Krolczyk, J. Y. Xu, A state of the art on surface morphology of selective laser-melted metallic alloys, Int. J. Adv. Manuf. Technol. 127 (2023) 1103–1142.
[31] W.G. Nan, M. Pasha, T. Bonakdar, A. Lopez, U. Zafar, S. Nadimi, M. Ghadiri, Jamming during particle spreading in additive manufacturing, Powder Technol. 338 (2018) 253–262.
[32] W.G. Nan, M. Pasha, M. Ghadiri, Numerical simulation of particle flow and segregation during roller spreading process in additive manufacturing, Powder Technol. 364 (2020) 811–821.
[33] R. Xu, W.G. Nan, Analysis of the metrics and mechanism of powder spreadability in powder-based additive manufacturing, Addit. Manuf. 71 (2023) 103596.
[34] K. Marchais, J. Girardot, C. Metton, I. Iordanoff, A 3D DEM simulation to study the influence of material and process parameters on spreading of metallic powder in additive manufacturing, Comput. Part. Mech. 8 (2021) 943–953.
[35] Z.W. Xiang, M.D. Zhang, R. Yan, Q. Yin, K.F. Zhang, Powder-spreading dynamics and packing quality improvement for laser powder bed fusion additive manufacturing, Powder Technol. 389 (2021) 278–291.
[36] A. Phua, P.S. Cook, C.H.J. Davies, G.W. Delaney, Powder spreading over realistic laser melted surfaces in metal additive manufacturing, Addit. Manuf. Lett. 3 (2022) 100039.
[37] P.S. Cook, A. Phua, C.H.J. Davies, G.W. Delaney, Modelling the influences of powder layer depth and particle morphology on powder bed fusion using a coupled DEM-CFD approach, Powder Technol. 429 (2023) 118927.
[38] H.P. Zhu, Z.Y. Zhou, R.Y. Yang, A.B. Yu, Discrete particle simulation of particulate systems: a review of major applications and findings, Chem. Eng. Sci. 63 (2008) 5728–5770.
[39] R.Y. Yang, R.P. Zou, A.B. Yu, Computer simulation of the packing of fine particles, Phys. Rev. E 62 (2000) 3900–3908.
[40] Q. Qian, X.Z. An, H.Y. Zhao, K.J. Dong, Y.L. Wu, H.T. Fu, H. Zhang, X.H. Yang, Particle scale study on the crystallization of mono-sized cylindrical particles subject to vibration, Powder Technol. 352 (2019) 470–477.
[41] Y. Tsuji, T. Tanaka, T. Ishida, Lagrangian numerical simulation of plug flow of cohesionless particles in a horizontal pipe, Powder Technol. 71 (1992) 239–250.
[42] K.L. Johnson, J.A. Greenwood, J.G. Higginson, The contact of elastic regular wavy surfaces, Int. J. Mech. Sci. 27 (1985) 383–396.
[43] R.D. Mindlin, Compliance of elastic bodies in contact, J. Appl. Mech. 16 (2021) 259–268.
[44] H.C. Hamaker, The London—van der Waals attraction between spherical particles, Physica 4 (1937) 1058–1072.
[45] R. Everaers, M.R. Ejtehadi, Interaction potentials for soft and hard ellipsoids, Phys. Rev. E 67 (2003) 041710.
[46] H. Chen, Q.S. Wei, Y.J. Zhang, F. Chen, Y.S. Shi, W.T. Yan, Powder-spreading mechanisms in powder-bed-based additive manufacturing: experiments and computational modeling, Acta Mater. 179 (2019) 158–171.
[47] Y. He, A. Hassanpour, A.E. Bayly, Combined effect of particle size and surface cohesiveness on powder spreadability for additive manufacturing, Powder Technol. 392 (2021) 191–203.